ARL-TR-8489 ● SEP 2018

US Army Research Laboratory

Morphological and Mechanical Characterization of Adolescent Yucatan Miniature Porcine Skull

by C Allan Gunnarsson, Stephen L Alexander, and Tusit Weerasooriya

NOTICES

Disclaimers

The findings in this report are not to be construed as an official Department of the Army position unless so designated by other authorized documents.

Citation of manufacturer's or trade names does not constitute an official endorsement or approval of the use thereof.

Destroy this report when it is no longer needed. Do not return it to the originator.

ARL-TR-8489 ● SEP 2018

US Army Research Laboratory

Morphological and Mechanical Characterization of Adolescent Yucatan Miniature Porcine Skull

by C Allan Gunnarsson and Tusit Weerasooriya
Weapons and Materials Research Directorate, ARL

Stephen L Alexander
SURVICE Engineering Company, 4695 Millennium Dr, Belcamp, MD

REPORT DOCUMENTATION PAGE

Form Approved
OMB No. 0704-0188

1. REPORT DATE *(DD-MM-YYYY)*	2. REPORT TYPE	3. DATES COVERED (From - To)
September 2018	Technical Report	June 2017–June 2018

4. TITLE AND SUBTITLE
Morphological and Mechanical Characterization of Adolescent Yucatan Miniature Porcine Skull

5a. CONTRACT NUMBER

5b. GRANT NUMBER

5c. PROGRAM ELEMENT NUMBER

6. AUTHOR(S)
C Allan Gunnarsson, Stephen L Alexander, and Tusit Weerasooriya

5d. PROJECT NUMBER

5e. TASK NUMBER

5f. WORK UNIT NUMBER

7. PERFORMING ORGANIZATION NAME(S) AND ADDRESS(ES)
US Army Research Laboratory
Weapons and Materials Research Directorate (ATTN: RDRL-WMP-B)
Aberdeen Proving Ground, MD 21005-5066

8. PERFORMING ORGANIZATION REPORT NUMBER
ARL-TR-8489

9. SPONSORING/MONITORING AGENCY NAME(S) AND ADDRESS(ES)

10. SPONSOR/MONITOR'S ACRONYM(S)

11. SPONSOR/MONITOR'S REPORT NUMBER(S)

12. DISTRIBUTION/AVAILABILITY STATEMENT
Approved for public release; distribution is unlimited.

13. SUPPLEMENTARY NOTES

14. ABSTRACT
Traumatic brain injury is the signature injury endured during the military conflicts in Iraq and Afghanistan resulting from blast and blunt/ballistic impact. Computational simulation based on realistic material models can be utilized to better understand the biomechanics of traumatic brain injury. To develop accurate material models, the material response of biological constituents, such as tissue and bone, must be understood. In addition, an in-depth evaluation of the micro-structural components of the skull and their response to mechanical loading may aid in understanding the mechanisms of injury. The current study examines the mechanical response and structural properties of the Yucatan minipig cranial bone (skull) to help develop material models inspired by its structure. This species is useful to study traumatic head injury because its gyroencephalic brain (hemispheres with convolutions) is more similar to the human brain than small animal models (i.e., rodents). However, this animal skull is uniform, which differentiates it from the human three-layer sandwich skull structure.

15. SUBJECT TERMS
Yucatan miniature porcine, skull morphology, mechanical characterization, digital image correlation, micro-X-ray tomography

16. SECURITY CLASSIFICATION OF:			17. LIMITATION OF ABSTRACT	18. NUMBER OF PAGES	19a. NAME OF RESPONSIBLE PERSON
a. REPORT	b. ABSTRACT	c. THIS PAGE			C Allan Gunnarsson
Unclassified	Unclassified	Unclassified	UU	42	19b. TELEPHONE NUMBER (Include area code) 410-306-1964

Contents

List of Figures v

List of Tables v

Acknowledgments vi

1. Introduction 1

2. Methods 3

2.1 Skull Specimens 3

2.2 Micro-Computed Tomography 5

2.3 Compressive Mechanical Loading 5

3. Results 6

3.1 Morphology 6

3.1.1 Bone Volume Fraction 6

3.1.2 Structural Arrangement 8

3.1.3 Bone Tissue Density 9

3.2 Compressive Mechanical Response 11

3.2.1 Apparent Elastic Modulus and Compressive Strength 13

3.2.2 Apparent Poisson's Ratio 14

3.3 Relating Morphology to Mechanics 14

3.3.1 Model Parameters 15

3.3.2 Relating Elastic Modulus to Morphology 16

3.3.3 Estimation of Bone Tissue Modulus 17

3.3.4 Modulus as a Function of Thickness 18

4. Discussion and Limitations 19

4.1 Similarity to Human Skull 20

4.2 Depth Dependence of BVF 21

4.3 Effect of Irradiation Absorption on Bone 21

5. Conclusions **22**

6. References **24**

Appendix. Individual Specimen Anisotropy Values **28**

List of Symbols, Abbreviations, and Acronyms **30**

Distribution List **32**

List of Figures

Fig. 1 Specimen extraction and characterization process 4

Fig. 2 Example of μCT data, including x-z image layer (middle) used for morphology analysis (16-02) 5

Fig. 3 BVF as a function of thickness location a) for each specimen and b) averaged for all specimens 7

Fig. 4 BVF as a function of position along thickness for adolescent Gottingen (Alexander 2016) and Yucatan skull averaged over all specimens 7

Fig. 5 Schematic of two different DA calculation scales 8

Fig. 6 Change in specimen mass during drying process 10

Fig. 7 Apparent density as a function of position along thickness (y-axis) averaged for all specimens 11

Fig. 8 Apparent stress–strain responses of compression specimens loaded in quasi-static compression for left camera 12

Fig. 9 Typical strain profile of Yucatan skull during compression (16-02 left camera at 25 MPa stress) 13

Fig. 10 Typical $\boldsymbol{\varepsilon}_{XX}$ vs $\boldsymbol{\varepsilon}_{YY}$ for Poisson's ratio calculation (specimen 16-04, RC) 14

Fig. 11 Schematic showing the modeling framework (Alexander 2016) 15

Fig. 12 Schematic showing the derivation of the stress–strain response of each layer 16

Fig. 13 Modulus of each layer plotted as a function of the layer's average value of BVF 17

Fig. 14 Modulus vs BVF of Yucatan minipig skull with power law assuming k parameter is constant across minipig breeds 18

Fig. 15 Modulus vs. thickness position of Yucatan minipig skull 19

List of Tables

Table A-1 Overall average and individual specimen DA and tDA 29

Acknowledgments

The authors would like to acknowledge the contributions of Karen Pizzolato of the US Army Research Laboratory (ARL's) Survivability/Lethality Analysis Directorate for providing the animal skulls with accompanying demographical data for these experiments.

The research reported in this document was performed in connection with contract W911QX-16-D-0014 with ARL. The views and conclusions contained in this document are those of SURVICE Engineering Company and ARL. Citation of manufacturer's or trade names does not constitute an official endorsement or approval of the use thereof. The US Government is authorized to reproduce and distribute reprints for Government purposes notwithstanding any copyright notation hereon.

1. Introduction

The understanding and mitigation of traumatic brain injury (TBI) is a very important goal of the research community. Over 235,000 service members were diagnosed with TBI from 2000 to 2011, and it is estimated that 1.7 million civilians sustain a TBI each year (MLP 2013). One form of TBI occurs when external mechanical forces act on the head. These applied forces affect pressure and strain in the hard and soft tissues of the skull and brain. Understanding the underlying mechanisms by which mechanical forces applied to the head, and therefore to its various tissues, induce TBI is crucial to head protection designed to mitigate TBI occurrence. Therefore, it is necessary to determine the strain and pressure thresholds for tissue injury to the head in response to applied mechanical loading.

TBI studies that use impact and blast loading to determine the effect of external mechanical loading on injury to live tissues are conducted on animals rather than humans. However, the applicability of insight gained from animal TBI impact and blast experiments relies on the ability to relate animal injury thresholds to the human anatomy. The relationship will depend on the mechanical response of the constituents of the human and animal head, among many factors. The skull is important, as its mechanical response determines the transfer of deformation and stress to the brain during accelerative loading. The mechanical response of the skull, in turn, is dependent on its unique microstructure. Therefore, quantification of both the mechanics and morphology of the animal skull are required to enable any critical injury thresholds identified in an animal TBI study to be compared with and scaled to other species, including human. Ongoing research at the US Army Research Laboratory (ARL) uses various breeds of miniature porcine as human surrogates in experiments designed to understand the mechanisms of brain injury caused by mechanical loading during head impact. These breeds include the Gottingen and Yucatan minipigs.

The macroscopic structure of the human cranium has previously been reported (Gibson and Ashby 1997; Mow and Huiskes 2005; Alexander et al. 2017). Adult human skull bone is a three-layer sandwich structure with outer and inner tables composed of dense cortical bone sandwiched around a middle layer, the diploë, which is porous trabecular bone. The classification of bone tissue as either cortical or trabecular is based on the tissue's porosity. Cortical (compact) bone is denser (porosity <30%), while trabecular (spongy) bone has higher porosity (>30%) (Charlebois et al. 2010). The degree of structural anisotropy in mature cranial human bone has also been characterized (Dempster 1967; McElhaney et al. 1970). Some studies have classified cranial human bone as structurally isotropic, indicating that there is no prevailing directional bias in the arrangement of the bone.

Dempster (1967) punctured decalcified human skull away from the orbital cavities and facial structures to visualize the dominant direction of collagenous fibers in the outer table. He concluded that the fibers had a random orientation in the skull. Similarly, McElhaney et al. (1970) could not discern dominant directions in the histology of each of the three cranial layers. These findings are supported by recent research (Alexander et al. 2017) that used high-resolution micro-computed tomography (μCT) visualization of the canal structure within the tables of the human skull. A lack of a dominant structural direction in cranial bone would be in sharp contrast to load-bearing bones, such as the femur. Previous studies have visualized the highly anisotropic structure of the femur, in which collagen fibers are hierarchically arranged into cylindrical structures known as osteons, which are predominately oriented in the loading direction (Sanborn et al. 2015).

The microstructure of the skull evolves significantly with age, from birth to maturity. Both human and porcine cranial bones at birth have a single layer of compact bone, with a separate porous layer formed with age (Margulies and Thibault 2000; Baumer et al. 2009). Furthermore, young human skulls have clearly identifiable grain patterns associated with fibrous orientation. These patterns make the immature specimens strongly anisotropic in contrast with the mature skull, which lacks such oriented structures (Coats and Margulies 2006).

The mechanical response of human (McElhaney et al. 1970; Hubbard 1971; Peterson and Dechow 2003; Motherway et al. 2009; Boruah et al. 2013; Rahmoun et al. 2014; Prot et al. 2015; Alexander et al. 2018) and large-breed porcine (Margulies and Thibault 2000; Baumer et al. 2009) skulls has also been studied in various loading configurations. Margulies and Thibault reported the modulus of human cranial bone loaded in three-point bending as increasing from approximately 800 MPa at 1 week of age to approximately 2.6 GPa at 6 months. Moduli from mature human crania tested in three-point bending ranged from 3.28 ± 2 GPa (Rahmoun et al. 2014) to 7.46 ± 5.39 GPa (Motherway et al. 2009). The mechanical response may become less dependent on bone orientation during maturation in conjunction with the loss of identifiable grain patterns. For example, the outer tables of mature specimens are only weakly anisotropic (Peterson and Dechow 2002; Peterson and Dechow 2003; Chung and Dechow 2011), while the mechanical response of young specimens strongly depends on grain orientation (McPherson and Kriewall 1980).

Large-breed pigs generally weigh more than 250 kg and their skull thickness ranges from 6 to 30 mm (Sauleau et al. 2009). The thickness and the microstructure of the various breed minipig skulls are known to significantly differ from that of the large-breed pig and are dependent on the weight of the animal. Previous human and large-breed porcine studies have shown that the mechanical response of the cranial

bone is strongly dependent on its microstructure and that this structure changes significantly during maturation (Margulies and Thibault 2000; Coats and Margulies 2006; Baumer et al. 2009). The microstructural differences between the minipig and the large-breed pig indicate that the existing mechanical response data from large-breed pigs may not be adequate for use in computational models of minipigs or for correlation to the human. The differences therefore emphasize the need for the structural and mechanical properties of the minipig skull to be independently characterized for each breed in use. The adolescent Gottingen minipig skull has been studied previously (Alexander et al. 2016). However, mechanical and structural characterization of the Yucatan minipig skull is lacking.

In this report the structure of a 32.5-week-old Yucatan minipig skull is quantified and related to its compressive mechanical response. Individual full-thickness specimens were extracted from the skull for characterization of the structure and compressive mechanical response. The porosity and arrangement of the bone along the through-thickness of the skull were quantified using μCT. The mean intercept length (MIL) and degree of anisotropy (DA) of the bone structure was obtained using μCT images to determine the degree to which the cranial bone is structurally isotropic. A subset of the skull specimens was then compressed in the through-thickness (depth) direction, normal to the outer surface of the skull, at a quasi-static loading rate. The full-field strain tensor on the specimen surface was measured using digital image correlation (DIC) during deformation. Moduli at different depths were calculated from the experimental measurements. An attempt was made to relate apparent moduli of the structure to the localized porosity measurement of the bone to determine the relationship of pure bone, the porosity percentage, and the apparent modulus. This could be used to predict the variation of modulus with depth, as studied previously with the Gottingen breed minipig (Alexander
et al. 2016). However, for this breed and age the skull was observed to have a relatively constant porosity along the skull thickness.

2. Methods

2.1 Skull Specimens

All specimens were extracted from the skull of a Yucatan minipig bred as part of an impact loading study at ARL to understand the injury thresholds for behind-helmet blunt trauma. All procedures were approved by the ARL Safety Office and carried out in accordance with the rules and regulations of the Institutional Animal Care and Use Committee of the Edgewood Chemical and Biological Center. The skull was extracted from a juvenile Yucatan minipig that was not used in the impact

study; the minipig was certified as originating from a US Department of Agriculture regulated herd and as being healthy and disease free. The minipig was 32.5 weeks old with a mass of 54.2 kg at the time of slaughter. Mature Yucatan minipigs typically have mass of 70–83 kg and typically take 1 year or more to reach maturity (Rozkot et al. 2015). After slaughter, the skull was extracted from the head and all soft tissue in and around the skull was removed. The skull was stored frozen.

A bone pathology saw (Exact 312, Exact Technologies, Inc.) was used to cut the skull into a smaller skull cap (Fig. 1a; ruler unit is inches). The skull cap was cut into a smaller region of extraction (ROE); this was μCT scanned to ensure that no nasal cavity pores were present (Fig. 1b). The ROE was dissected into nine individual full-thickness specimens (Fig. 1c). The black dot indicates the specimen top (outer) surface. These individual specimens measured approximately 8 × 8 mm at the outer surface and had a thickness of 10–12 mm. The distance between these top and bottom surfaces, normal to the top (skin-side) surface, is considered the thickness or depth dimension. The cut in the thickness dimension was made normal to the skull outer surface. The specimens were minimally wet-sanded to ensure flat and parallel top and bottom surfaces prior to any morphological or mechanical characterization. The specimens were immersed in Hank's Balanced Salt Solution (HBSS) after fabrication and stored at 4 °C.

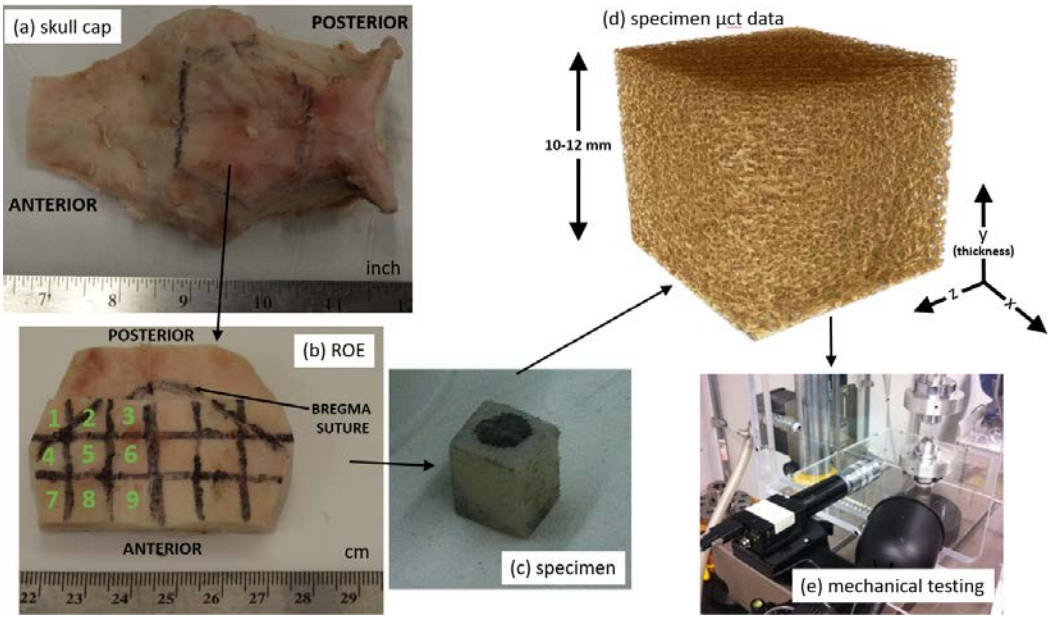

Fig. 1 Specimen extraction and characterization process

The individual specimens were labeled with the format XX-YY. The prefix XX identified the skull number; for this study, only a single skull was used, numbered 16. The suffix YY identified the individual specimen from each skull.

After the fabrication process, each of the nine specimens were characterized using µCT. A smaller cohort of those specimens was used for mechanical characterization in uniaxial compression experiments. This subset consisted of specimens 16-02, -04, -06, and -07 and will be referred to as the compression specimens.

2.2 Micro-Computed Tomography

The specimens were imaged prior to mechanical characterization using a µCT scanner (Bruker Skyscan 1172) with X-ray settings of 62 kV and 161 mA. The isotropic voxel size was 3.695 µm for all specimens. The specimen to source distance was 88.6 mm. Specimens were placed inside a 12.1-mm-diameter plastic tube and wrapped in HBSS-saturated gauze to maintain hydration during µCT scanning.

An image stack was reconstructed from the µCT data. The images stacked along the depth dimension (*y* in Fig. 1d), with each image representing a slice of the specimen having a thickness of 1 voxel. Each image plane represents the specimen cross section at a certain height (x-z in Fig. 1d). Figure 2 (middle) shows an example x-z slice from an image stack, as well as typical x-y and z-y slices (Fig. 2 left and right, respectively), where black represents pore and gray represents bone.

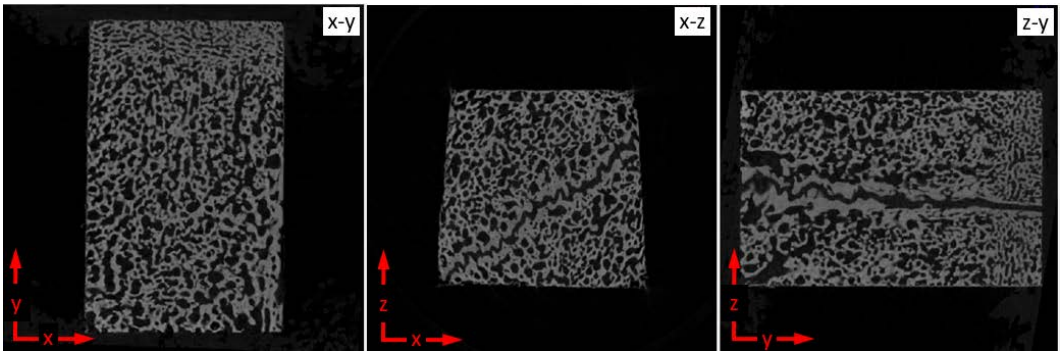

Fig. 2 Example of µCT data, including x-z image layer (middle) used for morphology analysis (16-02)

2.3 Compressive Mechanical Loading

Unconfined uniaxial compression was applied to each compression specimen in the thickness, or depth, direction. This loading direction was shown as the *y* dimension in Fig. 1d, and the loading direction is consistently referred to in this report as the *y* direction. The specimens were removed from storage just prior to compression, and two adjacent specimen surfaces were speckled for DIC. Specimens were loaded using an Instron servo-hydraulic load frame with a 5-kN load cell, as shown in

Fig. 1e. The time between removal from storage and mechanical testing was minimized to reduce specimen dehydration and resulting shape change; it took approximately 30 min for the speckle pattern to dry. The specimens were loaded under displacement control at a nominal strain rate of $10^{-3}s^{-1}$, as determined from physical measurement of the specimen thickness and controlled by the displacement rate of the test frame.

Two digital cameras (Point Grey Research, 12.0 MP, resolution 4 × 2.6 K) captured the 2-D deformation of two adjacent speckled specimen faces during loading. The two faces are henceforth referred to as the left camera (LC) and right camera (RC) sides. Postprocessing software (VIC-2D, Correlated Solutions) was used to calculate the 2-D displacements and strains from the deformation of the speckle pattern during loading.

3. Results

3.1 Morphology

The µCT images were analyzed to calculate bone volume fraction (BVF or f_{bv}) and to describe the structural arrangement of the bone within the skull specimens. The analysis was performed using software provided by the µCT manufacturer (Skyscan CT-Analyzer "CTan", Bruker). Prior to any quantification, images were first binarized using an automated algorithm (Otsu 1975) included within that software.

3.1.1 Bone Volume Fraction

The BVF was measured as a function of depth for the nine specimens extracted from the skull. The area ratio of bone to pore volume (V_f) was calculated for each image in the specimen image stack, creating a relationship between BVF and position along skull thickness. The area ratio for a given image (depth) was assigned as the value of the BVF at that depth. This assumes that the porosity along the thickness dimension is constant over the y distance of a single layer (voxel). Each 2-D image represents a 3-D space, with a thickness along the y axis of the voxel size. The morphology analysis of the Yucatan minipig skull specimens showed that the structure was highly porous, and that this porosity was relatively constant along the skull thickness dimension from the inner surface (closest to the brain, 0% thickness) to the outer surface (closest to the skin, 100% thickness).

Figure 3a shows the BVF as a function of thickness for the nine specimens from skull 16. Each specimen was normalized for depth, with 100% representing the outer surface and 0% the inner surface, regardless of the actual specimen thickness.

The BVF of each image slice was plotted as a function of thickness location from the inner surface to the outer surface. Figure 3b shows the BVF averaged over all of the specimens with error bars representing ±1 standard deviation.

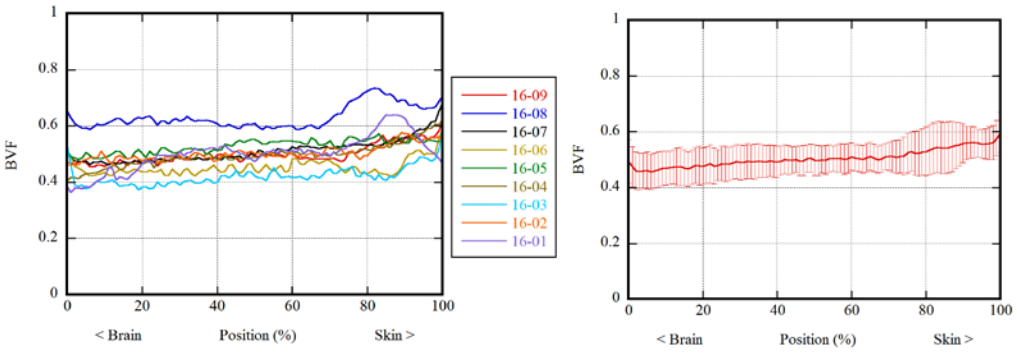

Fig. 3 BVF as a function of thickness location a) for each specimen and b) averaged for all specimens

As can be seen in Fig. 3, the BVF of the Yucatan pig is relatively constant, rising from 45% at the inner surface to 56% at the outer surface, with an average across all specimens of 50.6%. This is in contrast with the Gottingen minipig, which had a much larger change in BVF and saw the opposite trend, with BVF decreasing from inner to outer surface (Alexander et al. 2016). These differences are highlighted in Fig. 4, which shows the average BVF of both minipig breeds as a function of normalized thickness.

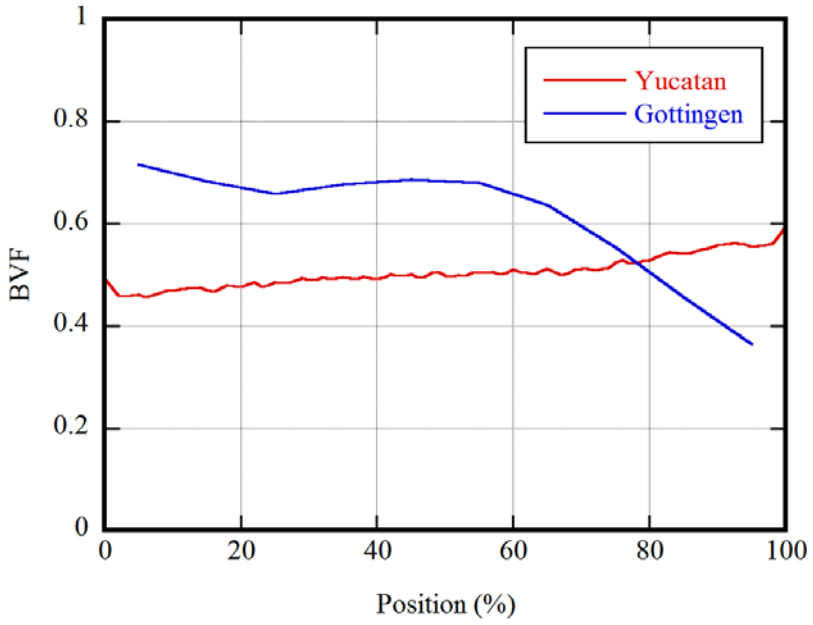

Fig. 4 BVF as a function of position along thickness for adolescent Gottingen (Alexander 2016) and Yucatan skull averaged over all specimens

3.1.2 Structural Arrangement

The structural arrangement of the skull bone within the individual specimen was quantified using the μCT datasets of the nine skull specimens. Volumes of interest (VOIs) with rectangular cross sections were extracted from each specimen's μCT dataset, such that each VOI contained almost all of the specimen volume while being entirely contained within the specimen surface. The VOI image stack was binarized, and the VOI anisotropy was calculated using the BoneJ add-in available for ImageJ, an image analysis software (Doube et al. 2010). The software calculated the components of the MIL tensor (Harrigan and Mann 1984) for each VOI; to do this, the software randomly sampled smaller spherical subvolumes within the VOI until the MIL results converged to a defined tolerance (this typically involved hundreds of such spherical samples). The principal axes of the MIL tensor are related to the principal axes of the bone phase averaged over the VOI. The DA was calculated, again in BoneJ based on the MIL tensor eigenvalues. These results varied slightly each time the analysis was performed; to ensure that the analysis was repeatable, it was performed 10 times for each specimen VOI.

DA is a unitless measure of how anisotropic a material is, from completely isotropic (i.e., a sphere filled with marbles) to highly oriented (i.e., a box of straight spaghetti noodles). There are two traditional methods of calculating DA using the MIL tensor. For both methods, a DA value that is lower indicates a less anisotropic structure; however, as DA approaches a value of 1, the two methods have opposite meaning. The scale difference between these two methods is shown in Fig. 5.

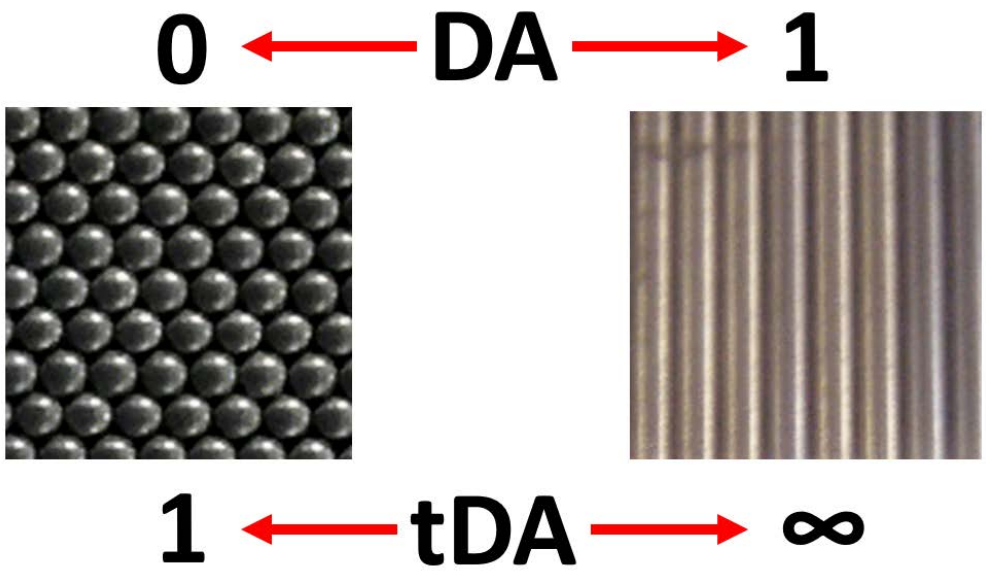

Fig. 5 Schematic of two different DA calculation scales

The first method uses a scale of 0 (perfectly isotropic) to 1 (perfectly anisotropic), and calculates DA as the ratio of the MIL tensor's smallest eigenvalue to the largest subtracted from 1 (Eq. 1). As the DA value increases, toward 1, the structure is more oriented.

$$DA = 1 - \frac{EV_{min}}{EV_{max}} \quad (1)$$

The second method of calculating DA uses a scale of 1 (perfectly isotropic) to infinity (perfectly anisotropic), where DA is the ratio of the largest eigenvalue to the smallest (Eq. 2). Here, as the DA value increases toward 1, the structure is less oriented. To differentiate between the two methods of calculating DA, *tDA* will be used to note the use of Eq. 2 to calculate DA (1 to ∞), as *tDA* is the nomenclature used by the BoneJ software to represent DA on the 1 to ∞ scale.

$$tDA = \frac{EV_{max}}{EV_{min}} \quad (2)$$

The DA results for the Yucatan minipig skull specimens are reported here using both scales; this is done to allow for comparison with other bone studies that may have reported DA calculated from only one of the scales. It is hoped that other researchers will follow this example and report DA results on both scales. This would be highly beneficial and increase the ability to make inter-study comparisons, because most of the literature report DA as an average derived from a cohort of specimens. While it is possible to convert the DA of a single structural analysis from DA to tDA or vice versa, it is not possible to convert a reported DA or tDA averaged across a cohort of specimens. The average DA for the nine Yucatan skull specimens was 0.348 ± 0.07; the average tDA was 1.549 ± 0.17. The individual specimen anisotropy values are tabulated in the Appendix.

3.1.3 Bone Tissue Density

The bone tissue density (ρ_b), which is the density of the actual bone material with zero porosity, is defined as the ratio of bone mass (m_b) to bone volume (V_b) as follows:

$$\rho_b = \frac{m_b}{V_b}. \quad (3)$$

Unfortunately, this cannot be measured directly from the specimens, as the specimen VOI includes both bone mass and fluid mass (m_f) that fill the pore volume. Additionally, the specimen volume (V_t) includes both bone volume and pore (V_f) volume.

$$m_b = m_t - m_f \quad (4)$$

$$V_b = V_t - V_f \quad (5)$$

The five specimens not used for compression experiments were removed from storage and dried in the laboratory atmosphere over several days, with periodic specimen mass measurements taken until each specimen's dried total mass (m_t^d) reached a constant value. This indicated that all of the fluid had evaporated from the pore space, and therefore the bone mass was equal to the specimen dried total mass as follows:

$$m_b = m_t^d. \tag{6}$$

The average specimen BVF (f_{bv}) is the ratio of bone volume to specimen volume, and was measured directly for each specimen using μCT (Section 3.1.1) as follows:

$$f_{bv} = V_b/V_t \rightarrow V_b = f_{bv}V_t. \tag{7}$$

Substituting Eqs. 6 and 7 into 3, the bone tissue density can be directly measured using the specimen dried total mass, the (undried) specimen volume, and the average specimen BVF as follows:

$$\rho_b = \frac{m_t^d}{f_{bv}\,V_t}. \tag{8}$$

The BVF measured in Section 3.1.1 was averaged for each specimen and used with the specimen dried total mass and specimen volume in Eq. 8 to calculate the average bone tissue density for each specimen. The average bone tissue density for the five Yucatan minipig skull specimens was 2.54 ± 0.62 $\frac{g}{cm^3}$. For comparison, the bone tissue density of the Gottingen minipig was measured to be 1.86 ± 0.10 $\frac{g}{cm^3}$ (Alexander et al. 2016). Figure 6 shows the change in mass during the drying period averaged for the specimens.

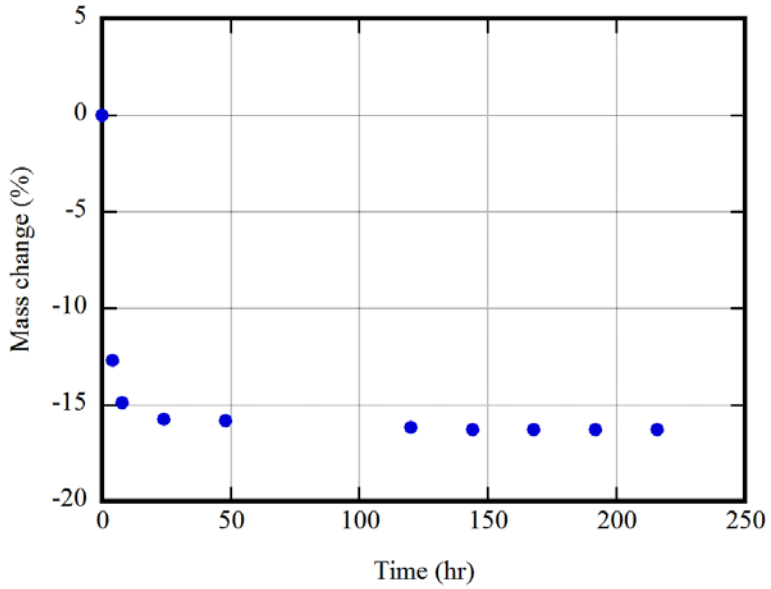

Fig. 6 Change in specimen mass during drying process

The averaged depth-dependence of the BVF for the nine specimens (see Fig. 3) was then multiplied by the bone tissue density to calculate a prediction of the apparent density (ρ_A) as a function of depth. Figure 7 shows the depth-dependent apparent density as a function of depth, which ranges from 1.16 to 1.50 $\frac{g}{cm^3}$, and has an average of 1.285 $\frac{g}{cm^3}$.

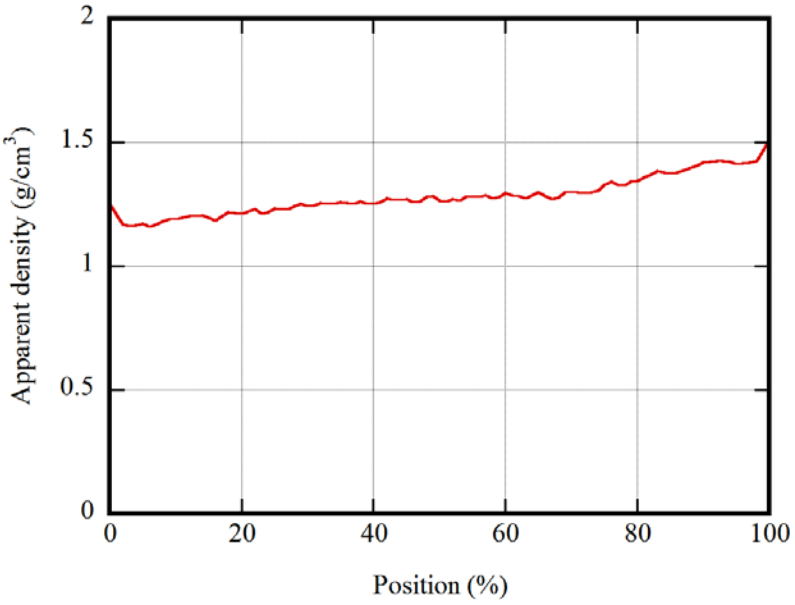

Fig. 7 Apparent density as a function of position along thickness (y axis) averaged for all specimens

3.2 Compressive Mechanical Response

The apparent farfield stress–strain behavior of the compression specimens is shown in Fig. 8 for the LC only, for clarity. The mechanical response obtained using the RC was virtually identical to that obtained using the LC. This stress–strain behavior represents the apparent compressive response of the Yucatan minipig skull as a structure.

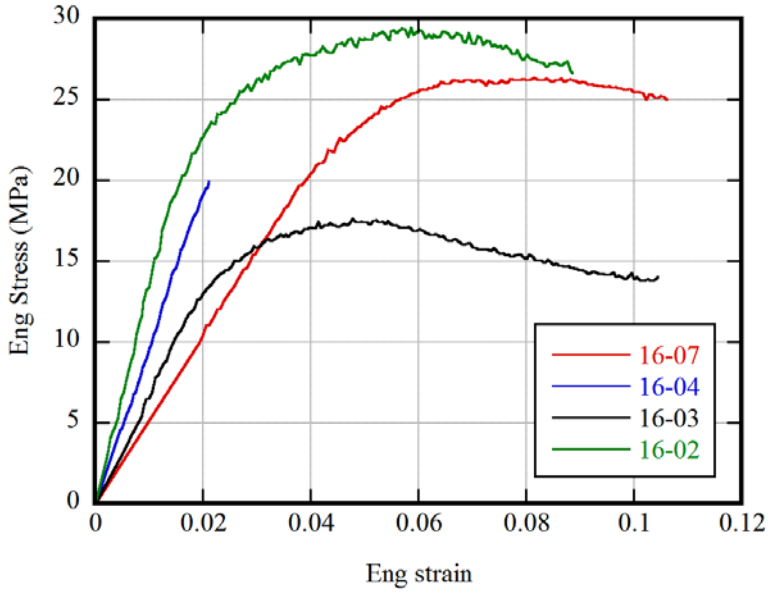

Fig. 8 Apparent stress–strain responses of compression specimens loaded in quasi-static compression for the LC

Engineering stress was calculated using the load cell output and undeformed cross-sectional area of the specimen, as measured with digital calipers. Apparent engineering strain was calculated using specimen deformation measured from the displacement of the compression platens. Platen displacement, as opposed to machine cross-head displacement, has been shown to be more accurate (Alexander et al. 2018), as it eliminates any machine compliance from the specimen deformation measurement. These methods of calculating stress from the load cell and strain from the platen displacement provided the macroscopic, or far-field, response of the specimen and will be referred to as apparent stress and apparent strain. Specimen 16-04 experienced a data acquisition failure midway through the experiment; however, sufficient data were collected to allow for determination of the apparent elastic modulus, so they are included here.

The DIC strain profiles measured on the specimen surfaces during compression were uniform. A representative compressive strain profile generated by DIC is shown in Fig. 9; this is for specimen 16-02 (LC) at stress of 25 MPa. There was no evidence of any strain concentration at any location on the specimen surface. This is expected; as BVF is relatively constant throughout the specimen thickness, the strain should be evenly distributed.

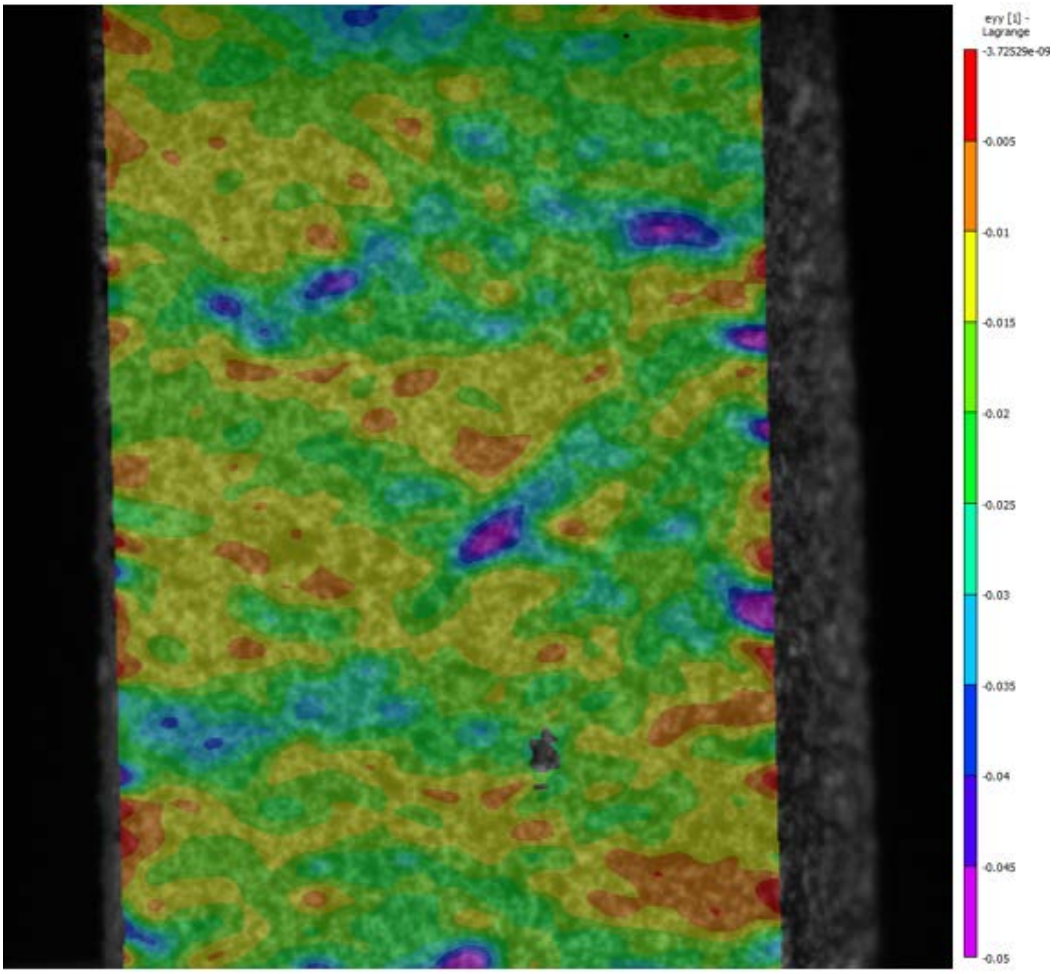

Fig. 9 Typical axial strain profile of Yucatan skull specimen during compression (16-02 LC at 25-MPa stress)

3.2.1 Apparent Elastic Modulus and Compressive Strength

The apparent elastic modulus was determined from the initial linear region of the stress strain response for each of the specimen–camera combination. The modulus measurement difference between cameras for a single specimen was very small. The average apparent modulus for all eight measurements was 880 ± 330 MPa and ranged from 505 MPa to 1.35 GPa. The apparent compressive strength was taken as the maximum apparent stress for the three specimens. The average apparent compressive strength was 24.3 ± 6.1 MPa.

3.2.2 Apparent Poisson's Ratio

The full-field strain data also allowed for the measurement of an apparent Poisson's ratio (ν), which is defined as the ratio of transverse strain (ε_{xx}) to axial strain (ε_{yy}) as follows:

$$\nu = \frac{\varepsilon_{xx}}{\varepsilon_{yy}}. \tag{9}$$

Both the axial and transverse strain were averaged over the entire specimen face for each time point. They were then related together, and a linear fit of the initial region ($0 \leq \varepsilon_{yy} \leq 0.02$) was used to calculate Poisson's ratio. The average Poisson's ratio for all eight datasets was 0.219 ± 0.040. The axial and transverse strain data used for one specimen to calculate Poisson's ratio are shown in Fig. 10.

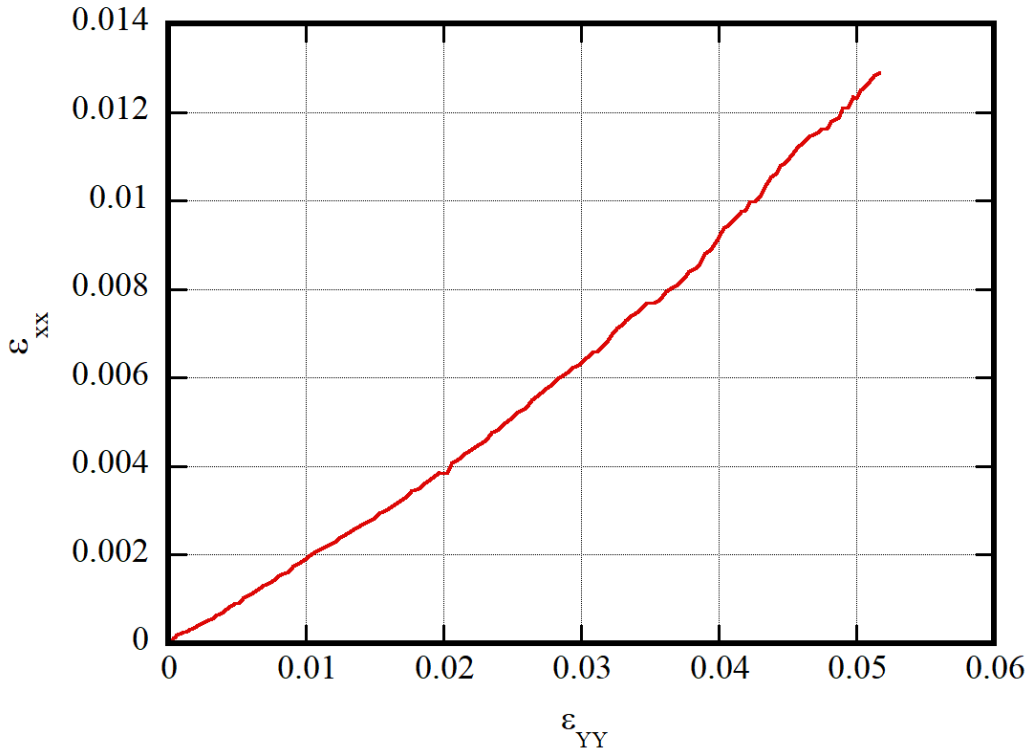

Fig. 10 Typical ε_{XX} vs. ε_{YY} for Poisson's ratio calculation (specimen 16-04, RC)

3.3 Relating Morphology to Mechanics

The lack of observable strain banding during compression, present in the Gottingen minipig skull (Alexander et al. 2016), reinforces the morphological results (Section 3.1) indicating that the morphology was constant throughout the thickness and did not effect a gradient in the mechanical response. This suggests that the skull may be represented as a single layer with uniform material properties. However, an

attempt was still made to model the skull specimens by discretizing the depth dimension into 10 layers acting in series so that an estimate of the bone tissue modulus (E_0) could be obtained. This modeling framework has been presented previously (Alexander et al. 2016) and is summarized here. The model is shown schematically in Fig. 11. For each layer, the morphology was approximated as constant with a single BVF value, f_{BV}^n. This single-layer BVF was calculated by averaging the depth-dependent BVF over the spatial volume of the layer.

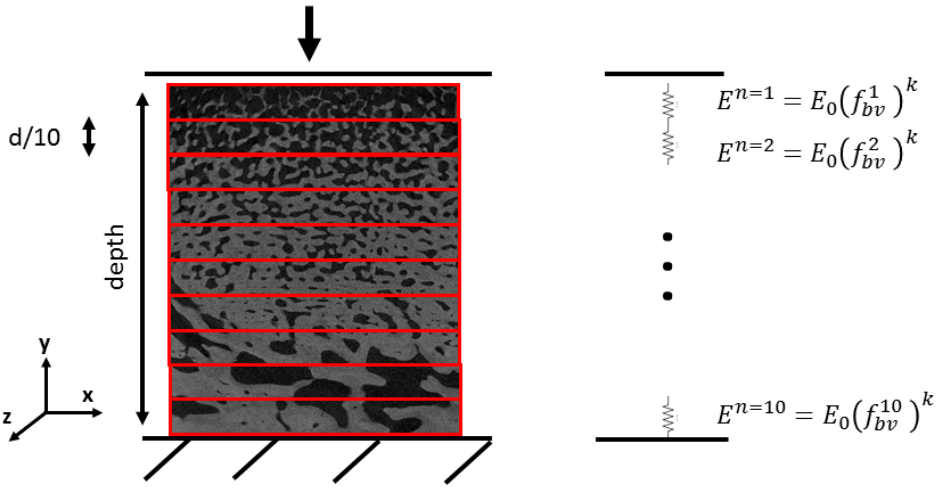

Fig. 11 Schematic showing the modeling framework (Alexander et al. 2016)

Each layer was modeled as also having a single apparent modulus (E^n). The layer's apparent modulus is related to the bone tissue modulus (E_0) of the bone phase (BVF = 1) by a power of the layer's average BVF as shown in Eq. 10.

$$E^n = E_0(f_{BV}^n)^k \tag{10}$$

3.3.1 Model Parameters

Two of the parameters from Eq. 10, E^n and f_{BV}^n, were experimentally derived for each layer. The other two parameters, E_0 and k, were to be found through fitting to the experimentally derived relationship between E^n and f_{BV}^n.

The average BVF value of each layer, f_{BV}^n, was directly calculated from the μCT data. The layer's apparent modulus, E^n, was obtained from the stress–strain response of each layer. The individual layer strain history (along the loading direction), ε_{yy}(t), was obtained for each layer by averaging the axial strain (ε_{yy}) over the *x*-*y* area of the layer at each time point using the DIC data (Vic-2D 2009, Correlated Solutions Inc.). This was repeated for all 10 layers.

Layer stress in the loading direction, $\sigma_{yy}(t)$, was assumed to be the specimen apparent stress (Section 3.2), $\sigma_{yy}^{n}(t) = \sigma_{yy}(t)$, as the layers of the specimen were modeled as acting in series.

The stress–strain response of each layer was obtained by matching the time domains of $\sigma_{yy}^{n}(t)$ and $\varepsilon_{yy}^{n}(t)$. A linear regression of the initial portion of the layer stress–strain response was performed to calculate the apparent elastic modulus of the layer, E^{n}. Figure 12 provides an example of obtaining the stress–strain response of the layers and their moduli, E^{n}. For clarity, the stress–strain response of only one of the 10 individual layers is shown. From the two specimen faces of the four compression specimens, the apparent elastic modulus was calculated for a total of 80 layers.

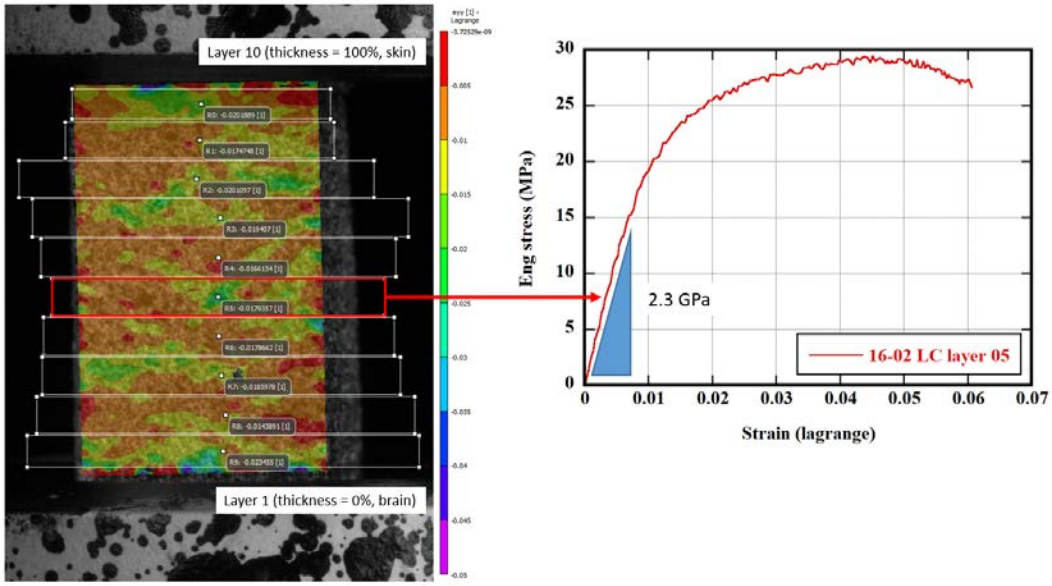

Fig. 12 Schematic showing the derivation of the stress–strain response of each layer

3.3.2 Relating Elastic Modulus to Morphology

Figure 13 shows the apparent modulus of each layer (E^{n}) of the Yucatan minipig skull specimens as a function of that layer's average BVF, f_{BV}^{n}.

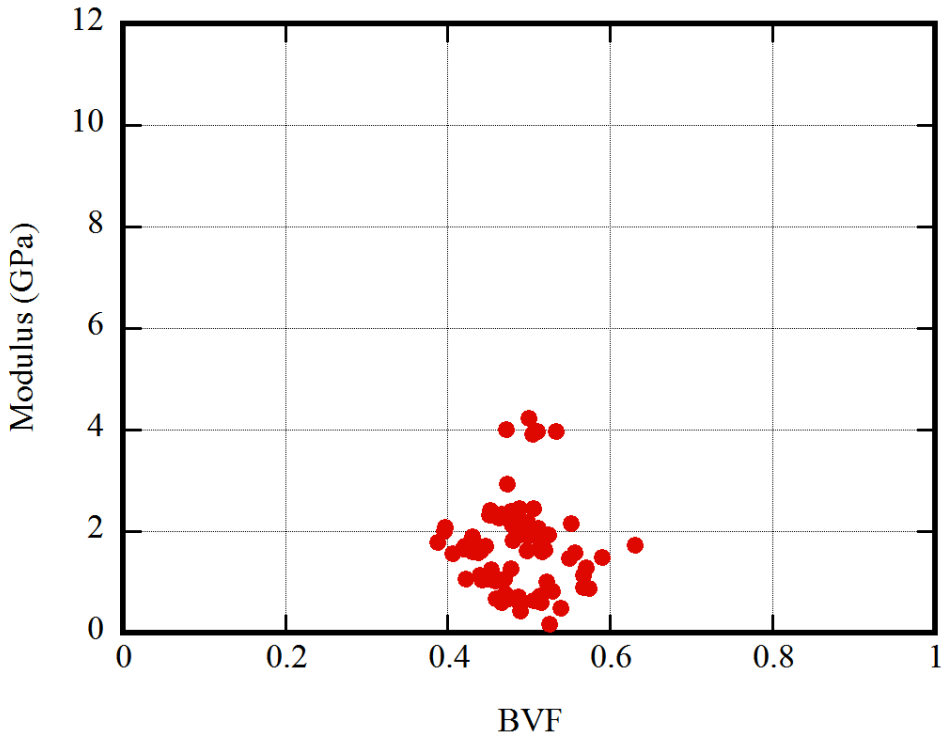

Fig. 13 Modulus of each layer plotted as a function of the layer's average value of BVF

It was not possible to fit the model parameters from Eq. 10 to the modulus-BVF data reported here. A nonlinear least square method was attempted for the fit; however, this generated a very small (approaching zero) value for k, indicating that BVF did not affect the layer modulus. This fit failure is expected trying to perform a fit over such a small range of BVF-based modulus values.

For the Yucatan minipig, the bone volume fraction is relatively constant through the skull thickness, thus the skull can be approximated as a single layer with a single apparent modulus for that layer. This allows for a much more simplified approach for models of the Yucatan minipig skull. This apparent modulus, obtained as an average of the moduli obtained for all 80 layers, is 1.87 ± 0.853 GPa. This apparent modulus represents the entire Yucatan skull structure, including porosity; it is not a direct representation of the bone tissue modulus (that is, modulus of the actual bone material with zero porosity).

3.3.3 Estimation of Bone Tissue Modulus

As discussed in the previous section, it was not possible to obtain a nonlinear least square fit to the layer moduli as a function of BVF; the range of BVF is too limited to provide a reasonable value for the parameter k. However, if k is assumed to be the same across minipig breeds, then the value of k obtained from previous research on the Gottingen minipig (Alexander et al. 2016), could be used to allow an

estimation of the Yucatan minipig bone tissue modulus. Substituting the averaged values of BVF (0.506, Section 3.1.1) and E_n (1.87 GPa, Section 3.3.2) from these results, and k (2.60 [Alexander et al. 2016]) into Eq. 10 allows a bone tissue modulus to be estimated for the Yucatan minipig skull (E_0) of 10.99 GPa. This is based on the assumption that the parameter k is constant across different minipig breeds, which may or may not be valid. Figure 14 shows the power law (Eq. 9) relationship between modulus and BVF for the Yucatan minipig skull assuming the k scaling factor is constant across minipig breeds.

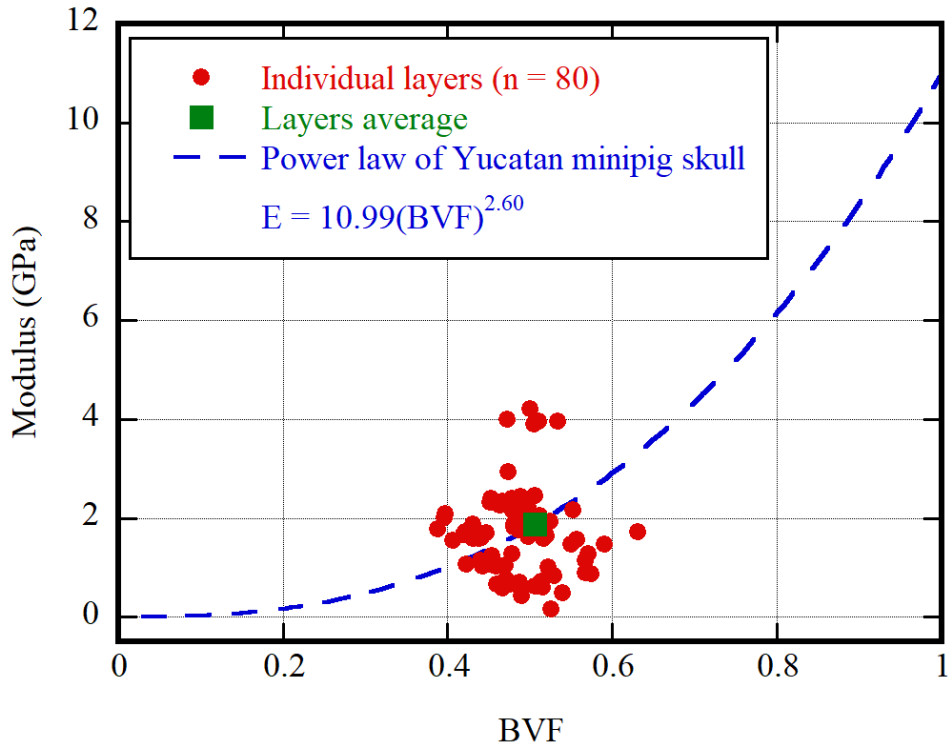

Fig. 14 Modulus vs. BVF of Yucatan minipig skull with power law assuming k parameter is constant across minipig breeds

3.3.4 Modulus as a Function of Thickness

The modulus as a function of location through the skull thickness was predicted by applying Eq. 10 to the averaged BVF–thickness relationship (Section 3.1.1). The predicted modulus is relatively constant along the skull thickness due to the unchanging BVF. The modulus–thickness relationship for Yucatan skull is shown in Fig. 15.

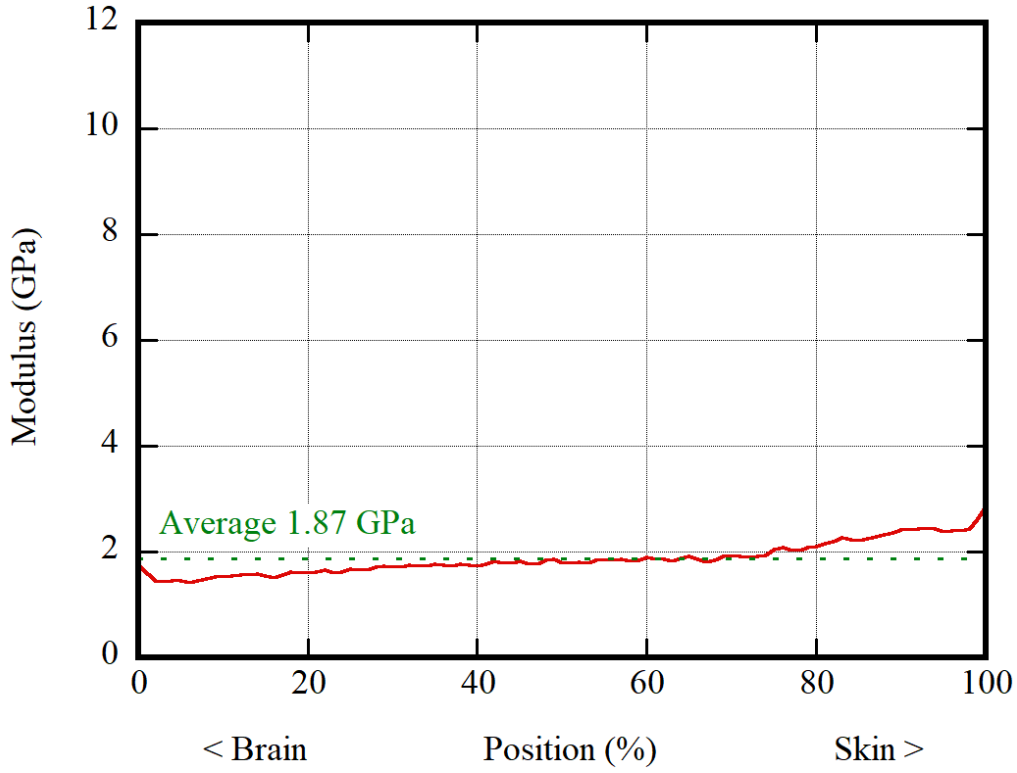

Fig. 15 Modulus vs. thickness position of Yucatan minipig skull

4. Discussion and Limitations

This study characterized the morphology of the adolescent Yucatan minipig cranium and measured its mechanical response to quasi-static compression. The information obtained from this study can be directly implemented into finite element models to improve simulation accuracy. Computational limitations restrict the amount of detail, such as pore structure, that can be accurately represented in a whole animal head model. As a result, solid elements often represent portions of the skull that are porous. Assigning microstructurally inspired material models for these elements, which intrinsically account for the biphasic mixture, would greatly improve the biofidelity of the model over simply using parameters derived for pure bone. Thompson et al. (2016) recently demonstrated that modeling the Gottingen minipig skull with a 10-layer system, using experimentally determined material properties for each layer, made a significant difference on the peak pressure experienced in the brain during simulations of head impact. Here it was determined that the Yucatan minipig skull structure is relatively constant over the thickness, simplifying the need for complex models.

The morphological and mechanical characterization reported here was performed on a limited number of samples originating from a single skull. Therefore, it is

difficult to state whether the results here are representative of other skulls from this age and breed. The mechanical response found here was obtained from only four specimens taken from a single skull. It would be ideal to have a larger sample size from which to draw statistical conclusions.

The stress–state during loading was approximated as consisting of uniaxial stress. For this to be valid, it would require that the specimen be perfectly machined to a parallelepiped with flat and parallel sides, which here is an approximation. For example, the stress–strain response of some layers had initial artifacts, likely due in part to irregular specimen geometries. Also, for the approximation to be valid, it would require that the bone material be aligned in the direction of loading. This is known to be not the case, causing the bone structure to be in a multiaxial, not uniaxial, stress state during compression.

The small-strain specimen response is assumed to be elastic, but this may not be the case. Other research (Alexander et al. 2016) has shown that when bone is loaded to small strains that are fully recovered after unloading, the recovery demonstrates significant hysteresis, indicating the possibility of significant viscoelastic effects. The layer-specific stress–strain responses were linear for only a small amount of strain and elasticity remained a first-order approximation. The range of the response used for fitting the elastic modulus was maintained as constant as possible, and layer strain of only several percent was used. Therefore, this modulus would not predict the response at higher strain values.

In estimating the bone tissue modulus, it was assumed that the scaling factor k in the power law relationship is an intrinsic material property that is constant across minipig breeds; however, there is no research available to directly support this assumption.

4.1 Similarity to Human Skull

Motivation for this study is based on the use of the Yucatan minipig as an adult human surrogate for blunt trauma research. Therefore, it is presupposed that, ideally, the Yucatan minipig skull should be as similar as possible to the human skull. The adult human skull has a layered structure, with two relatively dense outer layers (tables) sandwiched around a porous center layer (diploë). For the human skull, the table apparent density is approximately 1.8 g/cm^3 and the diploë apparent density ranges from 0.1 to 1.0 g/cm^3 (Mow and Huiskes 2005). The Yucatan minipig skull apparent density is relatively constant across the thickness at approximately 1.5 g/cm^3. This is similar to an average of the human skull layers; however, the Yucatan skull does not have a layered structure, which may significantly affect its mechanical response. The human skull, with its low-density

center layer, may be designed to crush early and absorb energy during skull impact that is not accurately represented by the Yucatan minipig skull.

4.2 Depth Dependence of BVF

The adolescent Yucatan minipig skull morphology was relatively constant in the skull through thickness direction. The bone along the inner surface gradually transitioned to slightly denser bone at the outer surface. The BVF changed marginally, from an average BVF at the inner surface of 46% to an average of 58% at the outer surface. This change was almost perfectly linear, with a rate of change of approximately 0.1% BVF per percent thickness.

4.3 Effect of Irradiation Absorption on Bone

The skull bone specimens used here for compression experiments were first characterized using a µCT to understand their structure and orientation. The µCT process causes the bone to absorb an irradiation dosage during exposure to the X-ray beam. There are studies that suggests that irradiation exposure may alter the mechanical properties of bone due to degradatory effects on the collagen (Anderson et al. 1992; Fideler et al. 1995; Hamer et al. 1996; Currey et al. 1997; Cornu et al. 2000; Vastel et al. 2004; Barth et al. 2010). Specifically, irradiation causes radiolysis of water, which can induce collagen cross-linking, decreasing plasticity, and increasing brittleness (Colwell et al. 1996). Most studies report a significant effect of irradiation dosage on the plastic collagen material properties with negligible effect on elastic properties. Barth et al. (2010) reported significant reduction in bending strength, plasticity, and fracture toughness in human cortical bone with increasing irradiation dosage, but no effect on bending stiffness. Currey et al. (1997) reported significant decreases in bending strength, work to fracture, and impact energy absorption with increasing irradiation dosage in human bone; however, the elastic modulus was unchanged.

To understand the effect of irradiation in this study, the dosage absorbed by each compression specimen was estimated using software provided by the manufacturer of the µCT scanner (CT-Ion, Bruker). This software estimates the irradiation dosage rate based on the applied voltage, source current, and source–object distance. For the scanning settings documented here (Section 2.2), the software provided an estimate of 2254 mGy/min. The specimen scans lasted 284 min, for a total dosage of 625 Gy. However, this estimates the irradiation dosage absorbed “in air”, and therefore the 625 Gy dosage corresponds to a worst-case estimate.

A more accurate estimate would account for X-ray depth attenuation caused by the specimen as well as the plastic tube enclosure, HBSS fluid, and gauze that

surrounded the specimen. As X-rays pass through a specimen they are attenuated, so the dosage rate is reduced at increased specimen depth (Poludniowski and Evans 2007). The CT-Ion software estimated that, for the same scan parameters, a 25-mm-diameter water column would experience a dosage rate of 234 mGy/min and a 75-mm-diameter water column would experience 71 mGy/min due to attenuation effects. These dosage rates are considerably lower than the corresponding 2,254-mGy/min "in-air" dosage rate and illustrate the strong effect of depth attenuation.

To estimate the actual dosage rate experienced by the specimen-fluid-gauze-tube system, it can be assumed as a 12.1-mm-diameter water column. Assuming that the in-air case represents an infinitesimal small-diameter water column and fitting a log relationship to the dosage rates supplied by the software for the three different diameter water columns, it is possible to extrapolate an estimated dosage rate for a 12.1-mm water column. This estimated dosage rate is 360 mGy/min, for a total dosage of 102 Gy. This is still an overprediction of the dosage received by only the bone specimen; a portion of the 102-Gy estimate is absorbed by the plastic tube, fluid, and gauze. An even more accurate (and lower) estimate would be obtained by predicting the absorbed dosage rate of an 8-mm-diameter water column (representing the bone specimen only) surrounded by a 12.1-mm-diameter water column (representing the tube, fluid, and gauze); however, this is not possible with the manufacturer software.

However, both the realistic depth-attenuation-corrected estimate of 102 Gy and the worst-case estimate of 625 Gy are still significantly less than the dosages that were shown to cause degradation of the plastic mechanical properties in human bone (10^2–10^3 kGy). Therefore, the effects of irradiation on the mechanical properties reported here for the Yucatan minipig skull are assumed to be negligible due to both the low dosage and the focus on elastic properties.

5. Conclusions

The morphology of the adolescent Yucatan minipig skull was quantified using µCT imaging with a resolution of several microns (3.695 µm). The volume fraction of the bone and its orientation within the skull were calculated from the imaging. The compressive mechanical response of cranial bone was also studied. In situ optical DIC methods were used to measure the 2-D strain distribution along the thickness on two adjacent specimen faces to enable a larger dataset. The morphology was observed to be relatively isotropic and constant along the through-thickness direction; this was observed in the mechanical response of the cranial bone as well.

The adolescent Yucatan minipig skulls had low variation in BVF across the skull thickness; the skull was slightly denser near the skin (58% BVF) and gradually transitioned to more-porous bone (46% BVF) near the brain. The average BVF was 50.6%. This arrangement diverged from previously reported studies on other miniature pig breeds, as well as adult humans, which both exhibit larger gradients in bone density along the thickness. The bone phase was observed in the μCT measurements to be relatively isotropic at the specimen length scale, similar to previous reports for human and pig skull.

The constant morphology of the Yucatan pig skull allows for the use of a simplified single-layer model, based on the apparent mechanical properties obtained by experiments conducted on specimens containing the entire thickness skull structure. This assumes structural and mechanical isotropy, which have been argued for here. The apparent modulus of the Yucatan skull is 1.87 GPa. The bone tissue modulus was predicted to be 10.99 GPa using the BVF–modulus relationship and assuming the scaling factor k to be constant across minipig breeds.

6. References

Alexander SL, Gunnarsson CA, Weerasooriya T. Structural influence on the mechanical response of adolescent Göttingen porcine cranial bone. Aberdeen Proving Ground (MD): Army Research Laboratory (US); 2016 Oct. Report No.: ARL-TR-7845.

Alexander SL, Rafaels K, Gunnarsson CA, Weerasooriya T. Morphological characterization of the frontal and parietal bones of the human skull. Aberdeen Proving Ground (MD): Army Research Laboratory (US); 2017 Mar. Report No.: ARL-TR-7962.

Alexander SL, Gunnarsson CA, Rafaels K, Weerasooriya T. Microstructural dependence of the compressive mechanical response of human skull. Aberdeen Proving Ground (MD): Army Research Laboratory (US); 2018; forthcoming.

Anderson M, Keyak J, Skinner H. Compressive mechanical properties of human cancellous bone after gamma irradiation. J Bone Joint Surg Am. 1992;74(5):747–752.

Barth H, Launey M, MacDowell A, Ager J, Ritchie R. On the effect of X-ray irradiation on the deformation and fracture behavior of human cortical bone. Bone. 2010;46(6):1475–1485.

Baumer TG, Powell BJ, Fenton TW, Haut RC. Age-dependent mechanical properties of the infant porcine parietal bone and a correlation to the human. J Biomech Eng. 2009;131(11):111006.

Boruah S, Henderson K, Subit D, Salzar R, Shender B, Paskoff G. Response of human skull bone to dynamic compressive loading. Proceedings of the International Research Council on Biomechanics of Injury (IRCOBI) Conference; 2013 Sep 11–13; Gothenburg, Sweden. Vol. 13; p. 497.

Charlebois M, Pretterklieber M, Zysset PK. The role of fabric in the large strain compressive behavior of human trabecular bone. J Biomech Eng. 2010;132(12):121006.

Chung DH, Dechow PC. Elastic anisotropy and off-axis ultrasonic velocity distribution in human cortical bone. J Anatomy. 2011;218(1):26–39.

Coats B, Margulies SS. Material properties of human infant skull and suture at high rates. J Neurotrauma. 2006;23(8):1222–1232.

Colwell A, Hamer A, Blumsohn A, Eastell R. To determine the effects of ultraviolet light, natural light and ionizing radiation on pyridinium cross-links in bone and urine using high-performance liquid chromatography. European Journal of Clinical Investigation. 1996;26(12):1107–1114.

Cornu O, Banse X, Docquier P, Luyckx S, Delloye C. Effect of freeze-drying and gamma irradiation on the mechanical properties of human cancellous bone. J Orthop Res. 2000;18(3):426–431.

Currey J, Foreman J, Laketic I, Mitchell J, Pegg D, Reilly G. Effects of ionizing radiation on the mechanical properties of human bone. J Orthop Res. 1997;15(1):111–117.

Dempster WT. Correlation of types of cortical grain structure with architectural features of the human skull. Amer J Anat. 1967;120(1):7–31.

Doube, Ml, Kłosowski MM, Arganda-Carreras I, Cordelières FP, Dougherty RP, Jackson JS, Schmid B, Hutchinson JR, Shefelbine SJ. BoneJ: free and extensible bone image analysis in ImageJ. Bone. 2010;47(6):1076–1079.

Fideler B, Vangsness T, Lu B, Orlando C, Moore T. Gamma irradiation effects on biomechanical properties of human bone – patellar tendon – bone allografts. American Journal of Sports Medicine. 1995;23(5):643–646.

Gibson LJ, Ashby MF. Cellular solids: structure and properties. Cambridge (UK): Cambridge University Press; 1997.

Hamer A, Strachan J, Black M, Ibbotson C, Stockley I, Elson R. Biomechanical properties of cortical allograft bone using a new method of bone strength measurement – a comparison of fresh, fresh-frozen and irradiated bone. Journal of Bone Joint Surgery. 1996;78(3):363–368.

Harrigan T, Mann R. Characterization of microstructural anisotropy in orthotropic materials using a second rank tensor. J Mat Sci. 1984;19(3):761–767.

Hubbard RP. Flexure of layered cranial bone. J Biomech. 1971;4(4):251–263.

Margulies SS, Thibault KL. Infant skull and suture properties: measurements and implications for mechanisms of pediatric brain injury. J Biomech Eng. 2000;122(4):364–371.

McElhaney JH, Fogle JL, Melvin JW, Haynes RR, Roberts VL, Alem NM. Mechanical properties of cranial bone. J Biomech. 1970;3(5):495–511.

McPherson GK, Kriewall TJ. The elastic modulus of a fetal cranial bone: a first step towards an understanding of the biomechanics of fetal head molding. J Biomech. 1980;13(1):9–16.

Motherway JA, Verschueren P, Van der Perre G, Vander Sloten J, Gilchrist MD. The mechanical properties of cranial bone: the effect of loading rate and cranial sampling position. J Biomech. 2009;42(13):2129–2135.

Mow VC, Huiskes R. Basic orthopaedic biomechanics and mechano-biology. 3rd ed. Baltimore (MD): Lippincott Williams & Wilkins; 2005.

[MLP] Multi-agency Leadership Panel (CDC, NIH, DoD, and VA). Report to Congress on traumatic brain injury in the United States: understanding the public health problem among current and former military personnel. Centers for Disease Control and Prevention (CDC), the National Institutes of Health (NIH), the Department of Defense (DoD), and the Department of Veterans Affairs (VA); 2013.

Otsu N. A threshold selection method from gray-level histograms. Automatica. 1975;11(285-296):23–27.

Peterson J, Dechow PC. Material properties of the inner and outer cortical tables of the human parietal bone. Anat Rec. 2002;268(1):7–15.

Peterson J, Dechow PC. Material properties of the human cranial vault and zygoma. Anat Rec A Discov Mol Cell Evol Biol. 2003;274(1):785–797.

Poludniowski G, Evans P. Calculation of X-ray spectra emerging from an X-ray tube. Part I. Electron penetration characteristics in X-ray targets. Med Phys. 2007;34(6 Part 1):2164-2174.

Prot M, Saletti D, Pattofatto S, Bousson V, Laporte S. Links between mechanical behavior of cancellous bone and its microstructural properties under dynamic loading. J Biomech. 2015;48(3):498–503.

Rahmoun J, Auperrin A, Delille R, Naceur H, Drazetic P. Characterization and micromechanical modeling of the human cranial bone elastic properties. Mech Res Commun. 2014;60:7–14.

Rozkot M, Václavková E, Bělková J. Minipigs as laboratory animals—review. Notes. 2015;9:2.

Sanborn B, Gunnarsson CA, Foster M, Moy P, Weerasooriya, T. Effect of loading rate and orientation on the compressive response of human cortical bone. Aberdeen Proving Ground (MD): Army Research Laboratory (US); 2015 May. Report No.: ARL-TR-6907.

Sauleau P, Lapouble E, Val-Laillet D, Malbert CH. The pig model in brain imaging and neurosurgery. Animal. 2009;3(8):1138–1151.

Thompson, KA, Sokolow AC, Ivancik J, Zhang TG, Mermagen WH, Satapathy SS. A sensitivity study of the porcine head subjected to bump impact. Proceedings of the ASME International Mechanical Engineering Congress and Exposition; 2016 Nov 11–17; Phoenix, AZ. p. V003T04A047–V003T04A047.

Vastel L, Meunier A, Siney H, Sedel L, Courpied J. Effect of different sterilization processing methods on the mechanical properties of human cancellous bone allografts. Biomater. 2004;25(11):2105–2110.

Appendix. Individual Specimen Anisotropy Values

Table A-1 tabulates the individual results for the nine specimens analyzed, as well as the overall averages. The single specimen values represent the average and standard deviation of the 10 degree of anisotropy (DA) analyses performed for each specimen.

Table A-1 Overall average and individual specimen DA and tDA

Specimen	DA		tDA	
	Average	**Std. deviation**	**Average**	**Std. deviation**
16-01	0.363	0.0097	1.571	0.0243
16-02	0.431	0.0157	1.758	0.0487
16-03	0.305	0.0100	1.440	0.0204
16-04	0.322	0.0066	1.474	0.0148
16-05	0.466	0.0081	1.871	0.0280
16-06	0.371	0.0090	1.590	0.0232
16-07	0.261	0.0104	1.354	0.0191
16-08	0.309	0.0055	1.446	0.0116
16-09	0.303	0.0073	1.434	0.0153
Average	0.348	0.0663	1.549	0.1693

List of Symbols, Abbreviations, and Acronyms

2-D	2-dimensional
3-D	3-dimensional
E_0	bone tissue modulus
E^n	apparent modulus
ε_{xx}	transverse strain
ε_{yy}	axial strain
μCT	micro-computed tomography
ρ_A	apparent density
ρ_b	bone tissue density
ν	Poisson's ratio
ARL	US Army Research Laboratory
BVF or f_{bv}	bone volume fraction
CT	computed tomography
DA	degree of anisotropy (0-1 scale)
DIC	digital image correlation
LC	left camera
m_b	bone mass
m_f	fluid mass
m_t^d	dried total mass
MIL	mean intercept length
HBSS	Hank's Balanced Salt Solution
RC	right camera
ROE	region of extraction
TBI	traumatic brain injury
tDA	degree of anisotropy (1-∞ scale)

VOI	volume of interest
V_b	bone volume
V_f	pore volume
V_t	specimen volume

1 (PDF) DEFENSE TECHNICAL INFORMATION CTR
DTIC OCA

2 (PDF) DIR ARL
IMAL HRA
RECORDS MGMT
RDRL DCL
TECH LIB

1 (PDF) GOVT PRINTG OFC
A MALHOTRA

11 (PDF) NATICK SOLDIER RSRCH DEV AND ENG CTR
M G CARBONI
D COLANTO
R DILLALLA
J FONTECCHIO
B KIMBALL
J KIREJCZYK
J PARKER
M MAFEO
M MARKEY
D PHELPS
J WARD

2 (PDF) PROG EXECUTIVE OFC SOLDIER
A FOURNIER
J MULLENIX

1 (PDF) MTRL SCIENCES DIV
LAWRENCE BERKELY NATL LAB
R RITCHIE

5 (PDF) SOUTHWEST RSRCH INST
C ANDERSON JR
S CHOCRON
D NICOLELLA
T HOLMQUIST
G JOHNSON

1 (PDF) INST FOR DEFNS ANLYS
Y MACHERET

4 (PDF) MRMC DOD BLAST INJURY RSRCH PROGRAM COOR OFC
R GUPTA
M LEGGIERI
T PIEHLER
R SHOGE

2 (PDF) MRMC JTAPIC PRGM OFC
W LEI
J USCILOWICZ

4 (PDF) US ARMY AEROMEDICAL RSRCH LAB
F BROZOSKI
V CHANCEY
B MCENTYRE
D WISE

1 (PDF) TARDEC
R SCHERER

1 (PDF) RDECOM HQ
AMSRD PE
D RUSIN

2 (PDF) EDGEWOOD CHEMICAL AND BIOLOGICAL RSRCH DEV AND ENG CTR
M HORSMON
N VINCELLI

1 (PDF) OSD DOT&E
J IVANCIK

5 (PDF) US NAVAL RSRCH LAB
A BAGCHI
A ILIOPOULOS
J MICHOPOULOS
K TEFERRA
X TAN

86 (PDF) ARL
RDRL CI
P PLOSTINS
RDRL DP
S WALSH
RDRL SL
P BAKER
RDRL SLB
G DIETRICH
RDRL SLB W
J GURGANUS
W MERMAGEN
S SNEAD
RDRL WM
A RAWLETT
S KARNA
S SCHOENFELD
RDRL WML F
G BROWN
RDRL WML H
T EHLERS
L MAGNESS

C MEYER
J NEWILL
D SCHEFFLER
B SCHUSTER
RDRL WML L
W OBERLE
RDRL WMM
J BEATTY
J MCCAULEY
J SINGH
M VANLANDINGHAM
RDRL WMM A
D O'BRIEN
T PLAISTED
K STRAWHECKER
E WETZEL
C YEN
RDRL WMM B
G GAZONAS
D GRAY
B LOVE
P MOY
T WALTER
V WU
RDRL WMM C
A BUJANDA
R JENSEN
J LA SCALA
RDRL WMM D
J SOUTH
J SIETINS
R CARTER
B CHEESEMAN
E CHIN
J SIETINS
RDRL WMM E
G GILDE
J LASALVIA
P PATEL
J SWAB
L VARGAS-GONZALEZ
RDRL WMM F
B DOWDING
S GRENDAHL
RDRL WMM G
J LENHART
K MASSER
R MROZEK
RDRL WMP A
S BILYK
RDRL WMP B
S ALEXANDER
A BROWN
A DAGRO
A DILEONARDI
A EIDSMORE
A GUNNARSSON
C HAMPTON
C HOPPEL
M KLEINBERGER
J MCDONALD
P MCKEE
K RAFAELS
M SCHEIDLER
K THOMPSON
T WEERASOORIYA
S WOZNIAK
T ZHANG
RDRL WMP C
S SATAPATHY
R BECKER
J BRADLEY
D CASEM
C MEREDITH
A SOKOLOW
RDRL WMP D
R DONEY
B SCOTT
C RANDOW
RDRL WMP E
M BURKINS
P GILLICH
M LOVE
P SWOBODA
RDRL WMP F
N GNIAZDOWSKI
R GUPTA
Y HUANG

UNIVERSITIES

3 (PDF) WHITING SCHOOL OF ENGRNG
JOHNS HOPKINS UNIV
T D NGUYEN
B NOTGHI
S BAILOOR

1 (PDF) COULTER DEPT OF BIOMED ENGRNG
GEORGIA INST OF TECH
S MARGULIES

1 (PDF) DEPT OF ENGRNG SCI AND MECHANICS
VIRGINIA POLYTECHNIC INST AND STATE UNIV
R BATRA

2 (PDF) MASSACHUSETTS INST OF TECHLGY
INST FOR SOLDIER NANOTECHNOLOGIES
R RADOVITZKY
S SOCRATE

1 (PDF) DEPT OF MECHL AND NUCLEAR ENGRNG
THE PENNSYLVANIA TATE UNIV
R KRAFT

1 (PDF) INDIAN INST OF TECH
R BHARDWAJ

1 (PDF) CENTER FOR APP BIOMECH
UNIV OF VIRGINIA
R SALZAR